Sintering of nanopowder based on an ordered phase with a perovskite-type $LaLuO_3:Yb^{3+}$ structure

Oksana Korniienko[1,2,3], Andrey Ragulya[1,2,3], Yuriy Yurchenko[1], Maryna Zamula[1], Oleksandr Shyrokov[1], Tamara Tomila[1], Tetiana Lobunets[1], Valeriy Kolesnichenko[1,*]

[1]*Frantsevich Institute for Problems of Materials Science of the NAS of Ukraine, O. Pritsaka Str. 3, Kyiv, 03142, Ukraine*

[2]*Nanotechcenter LLC, O. Pritsaka Str. 3, Kyiv 03142, Ukraine*

[3]*International Research Centre for Advanced Functional Nanostructured Materials and Technologies (IRC NANO), O. Pritsaka Str. 3, Kyiv 03142, Ukraine*

Received 26 December 2025; received in revised form 26 March 2026; accepted 29 March 2026

Abstract

The present work developed a methodology for synthesising single-crystal nanopowder based on an ordered phase with $LaLuO_3$ perovskite type structure. The $LaLuO_3:Yb^{3+}$ nanopowder, doped with 2 mol% Yb^{3+}, was synthesised by wet-chemical method from precursor nitrate solution and thermal treated to form pure perovskite phase. The synthesized nanopowder was comprehensively studied using IR spectroscopy, X-ray diffraction, scanning electron microscopy and adsorption-structural methods. The results of the X-ray diffraction analysis indicate that the synthesized powder is single-phase, with all the formed diffraction peaks corresponding to the ordered structure of the $LaLuO_3$ perovskite type. The unit cell parameters of the $LaLuO_3:Yb^{3+}$ (2 mol%) phase are: a = 0.6023 nm, b = 0.8385 nm, c = 0.5822 nm and V = 0.294 nm^3 whereas the average crystallite size is 51.2 nm. The nanopowder was consolidated using the spark plasma sintering (SPS) technique at 1380 °C and 50 MPa with dwell of 15 min, resulting in a fully dense ceramic material of 8.16 g/cm^3 (i.e. 99.54% theoretical density).

***Keywords**: $LaLuO_3:Yb^{3+}$, wet-chemical synthesis, spark plasma sintering, structural characterization*

I. Introduction

The accelerated advancement of scientific and technological pursuits necessitates the conception of novel materials that exhibit enhanced characteristics. Materials originating from oxide compounds, such as perovskite (ABO_3), have attracted substantial interest from researchers due to their readily manipulable physical and chemical properties, a property that can be effectively facilitated through the process of doping with rare earth and transition elements [1,2].

Compounds that contains two different rare earth elements ($LnLn'O_3$) in their structure were first mentioned in the 1960s [3,4]. These phases include a variety of compounds, including $LaLnO_3$, $LaYO_3$, $LnFeO_3$, $LnScO_3$, $LuAlO_3$ and others [5–9]. Since then, interest of scientific community in these materials has grown due to their physical and chemical properties. These compounds are suitable as electrolytes for electrochemical devices, such as solid oxide fuel cells (SOFCs), electrolysers, sensors, hydrogen separation membranes and electrochemical catalytic reactors [10–12] due to their high ionic conductivity and low activation energy. Additionally, $LaLuO_3$ based materials are being considered as replacements for silica (κ = 3.9) as the primary gate dielectric owing to their high κ value (above 40) [13]. Although a considerable number of publications have addressed the study of the materials with the ABO_3 perovskite structure, information pertaining to the phase, synthesis and sintering of $LaLuO_3$ based materials for laser applications remain limited, underscoring a need for further research. Laser ceramics are known have to include luminophores - the ions of rare earths, such as Yb^{3+}, Er^{3+} etc., which provide lasing properties in definite wavelength diapason.

Previous results on $LaLuO_3$ doped with Yb^{3+} ions have reported that besides the well-known emission spectrum in the IR region (920–1100 nm) from Yb^{3+}

*Corresponding author: tel: +380 935811938
e-mail: *kornienkooksana@ukr.net*

ions there is also a broad blue emission centred at 404 nm [14]. Kalusniak *et al*. [15] reported that in the laser experiments slope efficiencies of up to 75% were realised in a wide range of wavelengths between 1044 and 1123 nm. This indicates the potential of this new gain material for the generation of fs-pulses in mode-locked oscillators and for widely wavelength-tuneable lasers in the 1.1 μm wavelength range.

It is established that when an ordered structure, such as $LaLuO_3$ perovskite, is doped with REE cations, substitution can occur in both positions A or B [16–18]. Liu *et al*. [16] found that the exception is Pm^{3+} and Gd^{3+}, which are located exclusively in position A (Fig. 1). Consequently, when doping $LaLuO_3$ perovskite ordered structure with Yb^{3+} ions, substitution can be expected in both positions. In order to obtain a material with the specified characteristics, it is necessary that the substitution occurs in a specific site, especially for materials intended for luminescent applications. In accordance with the aforementioned results, we have tried to synthesised samples of an ordered perovskite-type structure in which substitution occurs preferable in position B. The expediency of allowing an ordered phase of the $LaLuO_3$ perovskite type with substitution at B site was also confirmed by data on the structure of phase equilibria in the three-component La_2O_3-Lu_2O_3-Yb_2O_3 system [19,20]. Given that a continuous series of solid solutions is formed in this system along the isoconcentrate of 50 mol% La_2O_3, it becomes possible to vary the amount of dopant and forming $La(Lu_{1-y}Ln_y)O_3$ compositions. Concurrently, in the development of materials exhibiting Ln^{3+} substitution in position A, with the general formula $(La_{1-x}Ln_x)LuO_3$, a relatively confined homogeneity region is anticipated, predicated on an ordered phase characterised by a perovskite-type structure. This, in turn, may result in the formation of a two-phase sample, a characteristic that may not always be advantageous in the context of material creation.

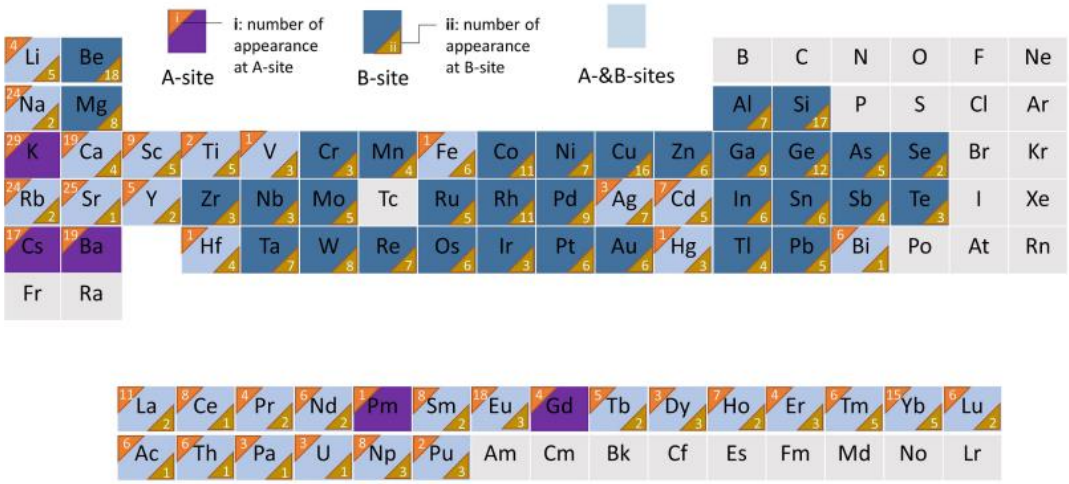

Figure 1. Substitution of REE cations at A and B-positions - cations occupying only A-positions (B-positions) are coloured purple (blue) and cations occupying both A- and B-positions are coloured blue (the number in the upper corner corresponds to the number of cations in the A-position, and the number in the lower corner corresponds to the number of cations in the B-position [3])

The development of high-quality nanopowders represents a crucial phase in the creation of novel ceramic materials. A range of synthesis methods are employed to create nanopowders based on an ordered phase with a perovskite-type structure, which have the general formula ABO_3. These methods include chemical co-precipitation [21], microemulsion [22], hydrothermal [23], solvothermal [24], microwave irradiation [25], spray pyrolysis [26], chemical vapour deposition [27] and the Pechini method [28]. Each method has been shown to contribute to the formation of a diverse morphology of nanopowders. In this study, the focus was on the development of a methodology for the synthesis of nanopowders based on an ordered phase such as $LaLuO_3$ perovskite doped with Yb^{3+} ions using the Pecini method.

The development of a methodology for sintering nanopowders is an equally important step in the creation of ceramic materials. Hot pressing (HP) and spark plasma sintering (SPS) are both sintering techniques that use heat and pressure to densify materials, but they differ in their heating methods. Hot pressing uses external heating elements to heat the entire sample, while SPS uses a pulsed direct current that passes through the material and dies to generate heat internally. This direct heating in SPS allows for faster heating rates, shorter processing times and lower sintering temperatures compared to hot pressing [29]. This sintering methodology can be used not only for nanopowders, but also for the direct synthesis of certain compounds [30–32]. Consequently, for sintering the effective method must be applied, which provides the rapid rate sintering technique to overcome

particle coalescence on heating, use of pressure to impede grain growth at low porosity, electric field and the use of additives that can accelerate shrinkage and impede grain growth [33]. This is a big challenge if the abnormal grain growth is inherent in perovskite-type materials at high temperatures. To get optically transparent, non-porous ceramics, a grain size of less than 100 nm is needed. Thus, the spark plasma sintering was selected as an advanced sintering technique, mostly corresponding to the as stated requirements.

II. Experimental

2.1. Powder synthesis

Doped nanopowder (with 2 mol% of Yb^{3+}) based on an ordered $LaLuO_3$ phase with a perovskite-type structure was synthesised by using the following reagents: La_2O_3, Lu_2O_3, HNO_3 (*puriss. spec.*), citric acid (*p.a.*), NaOH, isopropanol (*puriss.*). Preliminarily, 0.5 M solutions of $La(NO_3)_3$, $Lu(NO_3)_3$ and $Yb(NO_3)_3$, as well as a 1 M solution of citric acid were prepared. The nitrate solutions were mixed with citric acid and 10 ml of ethylene glycol under intensive stirring. After a certain period of time, 15 ml of 25% NH_4OH solution (or 4 ml of ethylenediamine) was slowly added and stirring was continued at a fixed temperature of ~90 °C for 15–20 min. The resulting solution was transferred to an oven for 3 days at 150 °C. Next, it was heat-treated in a muffle furnace (SNOL 1200) at 650–770 °C for 6 h at a temperature rise of 1 °C/min.

In the next step the synthesised powder was heat treated to obtain desirable crystalline product. The selection of calcination temperatures is related to the temperature of formation of an ordered phase with a perovskite-type structure and determined by derivatographic analyses. Based on derivatographic studies, the polymer complex formed by the citrate method undergoes thermal decomposition in multiple stages. This process is accompanied by endothermic effects up to 180 °C and exothermic effects in the temperature range 180–675 °C. At temperatures above 750 °C, another exothermic effect is observed, accompanied by a slight mass loss. Therefore, two series of heat treatment procedures were employed to find optimal calcination method. The first method involved subjecting the synthesised powder to a temperature of 675 °C for a duration of 6 h. The second method comprised a two-stage heat treatment process: in the stage 1 temperature was slowly increased (1 °/min) to 770 °C and in the stage 2 temperature was slowly decrease to 650 °C (for 6 h) and isothermal dwell at 650 °C for 6 h.

The resulting powder was then ground in a Fritch Pulverizetta ball mill in an isopropanol medium with zirconia balls (grinding media) at 250 rpm for different times. After separation of the balls from the suspension, the solvent was evaporated in a drying oven, then the resulting powder was ground in an agate mortar, pressed and sintered by spark-plasma sintering.

2.2. Sample sintering

The sintering of the powder heated with two-step regime (at 770°C/650°C) was carried out by using the pressure and the utilisation of a pulsed electric current, i.e. spark plasma sintering (SPS) on a FAST/SPS unit (FCT HP D 25/1, FCT Systeme GmbH, Germany) in a vacuum. The sintering regime consisted of three distinct stages. In the first stage the sample was rapidly heated (100 °C/min) up to 1230 °C with low pressing pressure (16 MPa). Then, the heating was continued up to 1280 °C with lower rate (25 °C/min) and at a higher pressure (50 MPa). In the third stage, the sample was heated (5 °C/min) up to the final temperature of 1380 °C (at 50 MPa) and hold at this temperature 15 min. The sintered sample was annealed in a laboratory furnace SNOL at temperatures of 1100 °C for 4 h and 24 h. Cooling was conducted inside the furnace.

The sintered samples were subjected to mechanical treatment (sandblasting). Two-sided plane-parallel polishing of the samples was performed on a grinding and polishing machine “Buehler Gmbh” (Germany). Carbide-silicon abrasive paper with a grit size ranging from 320 to 1200 was used for processing, after which the samples were polished with diamond pastes with a grain size of up to 1 μm.

2.3. Characterization methods

Infra-red spectroscopy study of the calcined nanopowder was conducted using a FTIR spectrometer (FSM-1201) within the wavelength range of 4000–400 cm^{-1}. The classical tablet technology and the two-beam measurement method were employed. The sample was thoroughly mixed with KBr powder in a ratio of 1:300 mg and the resulting mixture was pressed into transparent tablets with a diameter of 13 mm. The transmittance of the samples was measured relative to air. The samples were placed in the device, with the diameter of the sample holder window.

The phase composition of the obtained samples was determined by powder X-ray diffraction (XRD) using a SmartLab SE diffractometer (Rigaku, Japan) with CuKα radiation in continuous recording mode with a scanning speed of 10 °/min in the range of 2θ angles from 10° to 90°. The diffraction patterns were processed using the SmartLab Studio II software package with the data from [34]. The average crystallite size (D_{xrd} of the nanopowder was calculated using the Scherrer formula [35]:

$$D_{XRD} = \frac{0.9 \cdot \lambda}{\beta \cdot \cos\theta} \quad (1)$$

where λ is the X-ray wavelength (λ = 0.15418 nm), β is the peak width at half maximum (FWHM) and θ is the diffraction angle.

The porous structure of the obtained powder samples was studied by the adsorption-structural method using the ASAP 2000M (Accelerated Surface Area and Porosimetry System). The isotherms were then interpreted and used to calculate general porosity characteristics, including: total pore volume (V_{total}), specific surface area (S_{BET}, calculated by the BET method), total volume (V_{me}), surface of mesopores (S_{me}), differential distributions of mesopore volume and surface (calculated according to the BJH theory) and average equivalent pore diameter (D_{mean}, calculated according to the BET and BJH theories). The measurement range of this method is in the range of equivalent pore sizes from 0.3 to 300 nm [36–40].

The density of the sintered samples was determined by hydrostatic weighing using the Archimedes' method using formula [39].

$$\gamma = \frac{F_1 \cdot \gamma_B}{F_2 - F_3} \quad (2)$$

where F_1, F_2, F_3 are the mass of the sample in air, mass of the soaked sample in air, mass of the wet sample in water (respectively), and $\gamma_в$ is the water density.

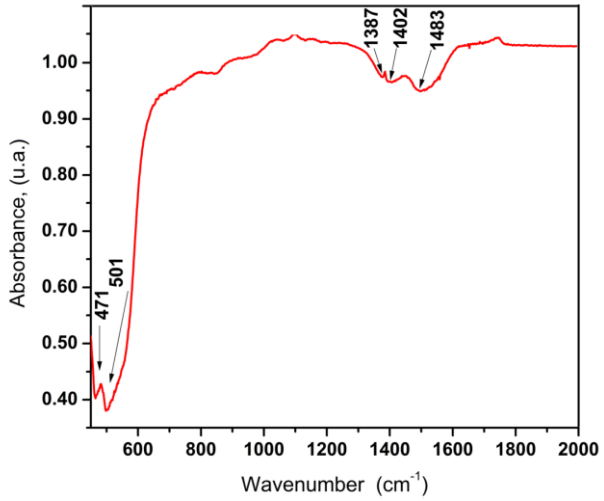

Figure 2. FTIR spectrum of the calcined $LaLuO_3$:Yb^{3+} (2 mol%) powder

III. Results and discussion

3.1. Structure of calcined powder

FTIR spectra analysis revealed the presence of absorption bands in the frequency range ν ~650–450 cm^{-1}, which correspond to M-O vibrations, where M = La, Lu (Fig. 2). Furthermore, the absorption bands in the frequency range ν ~1600–1300 cm^{-1} are indicative of the vibrations of carbonate ions in different coordination (monodentate and bidentate). Two peaks with frequencies ν ~ 468 and 501 cm^{-1} are suggestive of the crystallisation process of the perovskite-type structure $LaLuO_3$:Yb^{3+} (2 mol%).

X-ray phase analysis of the synthesized powder following heat treatment at 675 °C reveal the development of an ordered phase with a perovskite-type structure in amount of 94.6 wt.% accompanied by 5.4 wt.% of amorphous phase (Fig. 3). Consequently, the data presented indicates that the selected heat treatment regime for the synthesised powder does not result in complete crystallisation of the ordered perovskite structure, and the presence of the amorphous phase during sintering can adversely affect the density of the material obtained. The parameters determined from XRD analyses, of the nanopowder calcined at 675 °C, are: a = 0.6026 nm, b = 0.8396 nm, c = 0.5825 nm and V = 0.2947 nm^3, whereas the average crystallite size D_{xrd} = 53.3 nm and ρ_{xrd} = 8.16 g/cm^3. Due to the inability to obtain a fully crystalline sample, a slight alteration was made to the heat treatment regime of the synthesised powder. Thus, the diffraction pattern of the nanopowder following two-stage heat treatment process 770°C/650°C confirms the formation of pure crystalline perovskite phase. Table 1 shows the crystallographic parameters of the ordered perovskite-type structure that were determined by the Rietveld method. The unit cell parameters of the sample heated in two-stage 770°C/650°C process are: a = 0.6023 nm, b = 0.8385 nm, c = 0.5822 nm and V = 0.294 nm^3, whereas the average crystallite size and density are D_{xrd} = 51.2 nm and ρ_{xrd} = 8.175 g/cm^3, respectively. The obtained results indicate that the powders exhibited comparable crystallite sizes (53.3 and 51.2 nm), but in our opinion, the two-stage heat-treated nanopowder demonstrates a technologically advanced property due to its absence of an amorphous phase. Consequently, further studies were conducted on the nanopowder with a completely crystalline structure. The microstructural (SEM) study of the calcined nanopowder revealed the formation of particles with sizes ranging from 41 to 60 nm (Fig. 4).

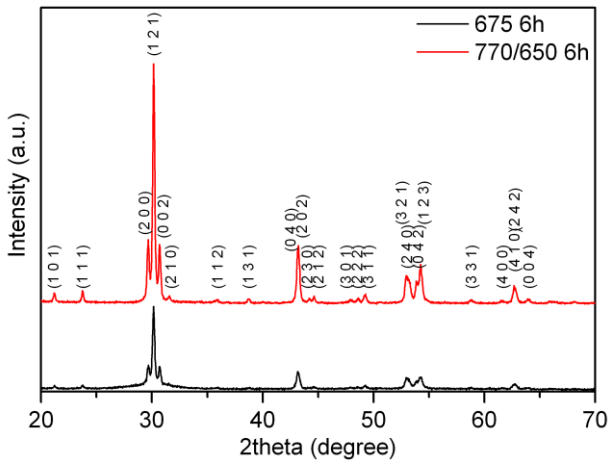

Figure 3. XRD patterns of $LaLuO_3$:Yb^{3+} (2 mol%) nanopowder heat treated at 675 °C and 770/650 °C

Table 1. Bond lengths Lu–O and angles O–Lu–O

Bond type	Bond length [Å]
Lu–O(1) × 2	2.225(6)
Lu–O(2) × 2	2.204(18)
Lu–O(2) × 2	2.226(18)
O1–Lu–O1	180.0(0)
	Bond angle [°]
O1–Lu–O2 × 2	86.8(7)
O1–Lu–O2 × 2	87.9(7)
O1–Lu–O2 × 2	92.1(7)
O1–Lu–O2 × 2	93.2(7)
O2–Lu–O2 × 2	88.2(3)
O2–Lu–O2 × 2	91.8(3)
O2–Lu–O2 × 2	180.0(0)

Low-temperature nitrogen adsorption studies (Fig. 5) of the obtained powder sample, heated to 770 °C followed by a decrease in temperature to 650 °C, confirmed its nanodispersed mesoporous (type IV) structure (according to the IUPAC classification, hysteresis loop type H3). The average particle diameter, calculated from the specific surface area (S_{BET}) using the formula $d = 6/(\rho \cdot S_{BET})$, is 90 nm (Table 2). Specific surface area (S_{BET}) is sufficiently high compared with the external surface area (S_{exter}). This suggests the occurrence of large defective particles. Which is substantiated by the size of the mesopores (~30 nm), and their defectiveness, with pores measuring 7 nm. Thus the adsorption-structural studies could indicate that the powder obtained following a two-stage heat treatment process exhibits slightly larger particles in comparison to the powder resulting from a one-stage heat treatment at 675 °C. This observation can be attributed to the fact that during the heat treatment process, there is an aggregation of small particles by their side faces, which results in the formation of larger combinations, such as agglomerates (Fig. 4).

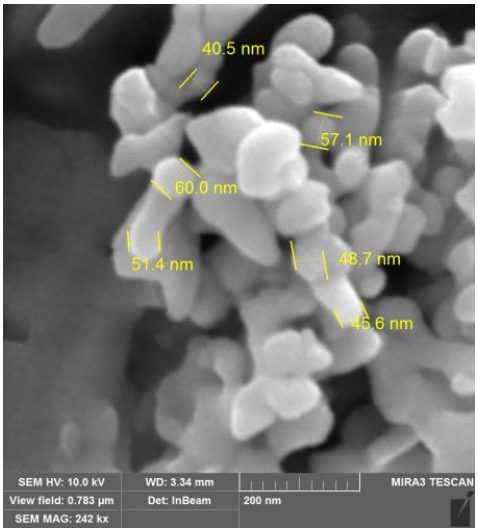

Figure 4. SEM images of $LaLuO_3:Yb^{3+}$ (2 mol%) nanopowder after heat treatment at 770 °C followed by a temperature decrease to 650 °C and dwell time for 6 h

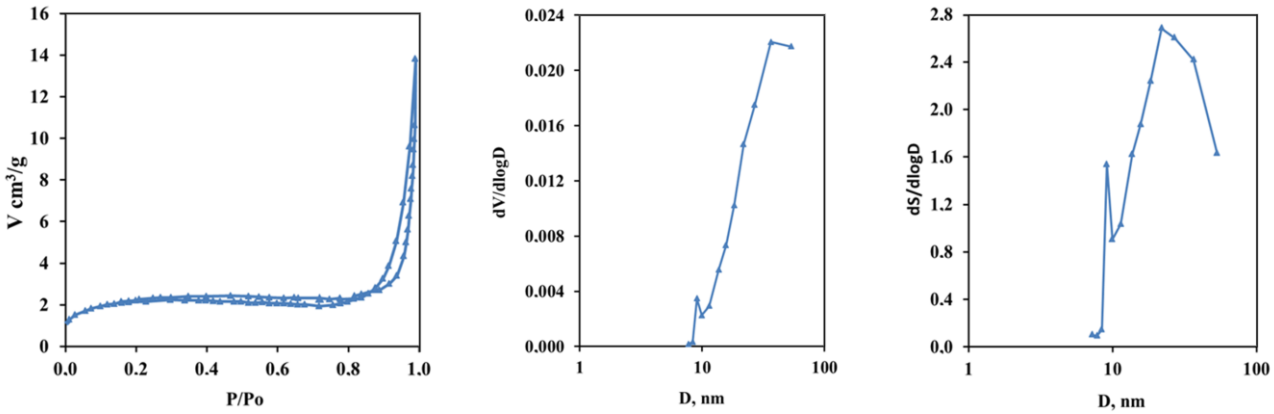

Figure 5. Low-temperature nitrogen sorption isotherm (a) and differential distributions of mesopore volumes (b) and surface areas (c) of $LaLuO_3$:2%Yb^{3+} sample after two-step heat treatment at 770°C/650°C

Table 2. General characteristics of $LaLuO_3:Yb^{3+}$ (2 mol%) porous structure nanopowder after two-step heat treatment at 770°C/650°C

V_Σ	t-method			BET		BJH adsorption			BJH desorption		
[cm³/g]	S_{exter} [m²/g]	S_{mi} [m²/g]	V_{mi} [cm³/g]	S_{BET} [m²/g]	D_{mean} [nm]	V_{me} [cm³/g]	S_{me} [m²/g]	$D_{mean\text{-}me}$ [nm]	V_{me} [cm³/g]	S_{me} [m²/g]	$D_{mean\text{-}me}$ [nm]
0.0135	0.076	7.92	0.0037	7.99	6.8	0.0139	2.08	26.7	0.0135	1.83	29.4

3.2. Structure of sintered samples

To obtain a dense ceramic material, the heat treated nanopowder was densified by using spark plasma sintering (SPS) technique. Densification behaviour was firstly investigated by the non-isothermal regime with a constant heating rate of 100

°C/min and constant pressure of 16 MPa. The relative density curve is presented in Fig. 6. As it is evident from Fig. 6, the shrinkage starts at 1100 °C and finishes at 1380 °C. This sintering regime was modified using our previous experiences [31]. Thus, the rapid heating rate regime of the SPS under minimal applied pressure was provided to overcome particle coarsening by coalescence on the initial stage of heating up to 1230 °C. In the second stage (up to 1280 °C) the heating rate was decreased to 25 °C/min and pressure increased to 50 MPa to allow breaking of agglomerates and rearrangement of nanoparticles into denser package. The proposed regime for pressure application enhanced the efficiency of densification and the sample underwent linear shrinkage of 7.26 mm (i.e. 73.7%) during sintering, which corresponds to density increase to ~99.5 %TD. To impede grain growth at low residual porosity, the slow heating rate regime and gradually growing pressure was used. It is worth noting that the slow heating rate regime of 5 °C/min in the range from 1280 to 1380 °C followed by 15-minute dwell ensures the effective healing of residual porosity. The shrinkage during the holding stage was only ~0.8% and resulted in reduction in porosity of 0.3%. The employment of the sintering regime in this study facilitated the acquisition of a dense sample at a reduced sintering temperature, i.e. 1380 °C, in contrast to 1450 °C utilized in another similar work [31].

It is also important to mention that the observed change of gas pressure within the working chamber of merely 0.02 hPa in the temperature ranges of 380–660 °C and 760–970 °C indicates elimination of some gases accompanying the sintering process.

The X-ray diffraction pattern of the sintered sample indicates the presence of diffraction peaks that correspond to an ordered perovskite-type structure (Fig. 7). The unit cell parameters are as follows: a = 0.6014 nm, b = 0.8379 nm, c = 0.5822 nm and V = 0.2934 nm^3, whereas the average crystallite size and density are D_{xrd} = 109.1 nm and ρ_{xrd} = 8.194 g/cm^3, respectively. The density of the sintered sample, as determined by hydrostatic weighing according to the Archimedes technique, is ρ = 8.163 g/cm^3, corresponding to 99.55 % of the theoretical value.

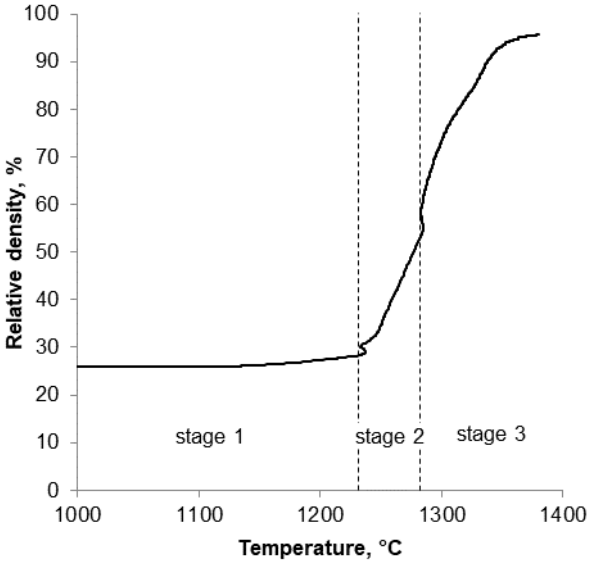

Figure 6. Relative density (%TD) during sintering of $LaLuO_3:Yb^{3+}$ (2 mol.%) composition

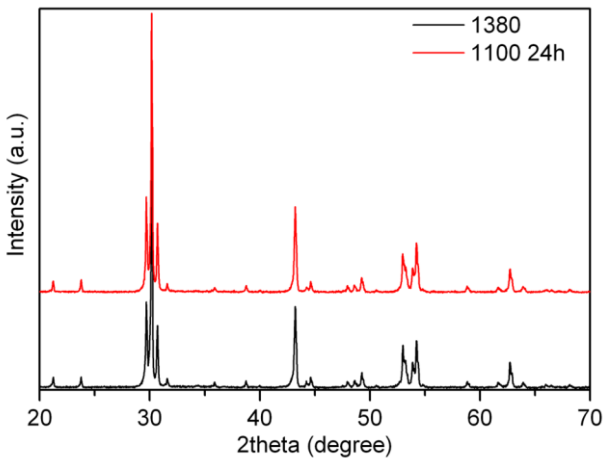

Figure 7. Diffraction patterns of sintered and annealed samples of $LaLuO_3:Yb^{3+}$ (2 mol%)

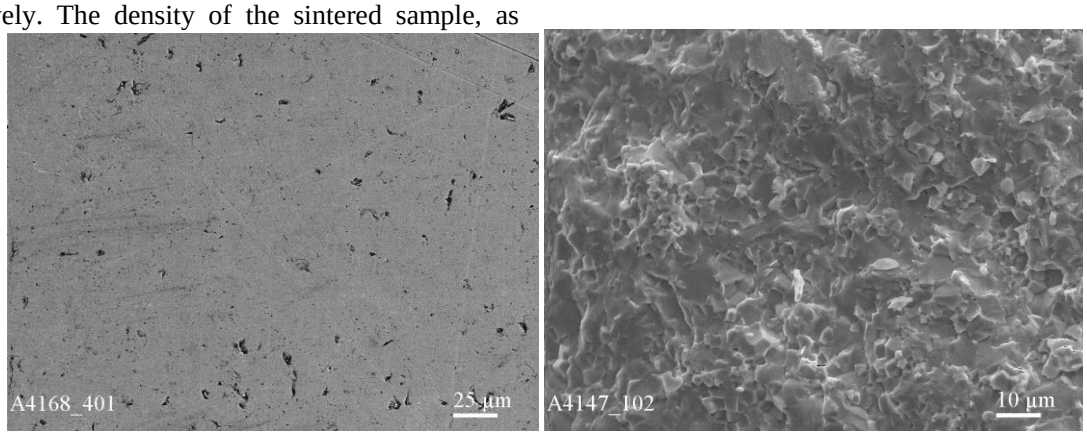

Figure 8. SEM micrographs of the sintered $LaLuO_3:Yb^{3+}$ (2 mol%) sample by SPS at 1380 °C, 15 min of the: a) polished surface and b) fracture surface

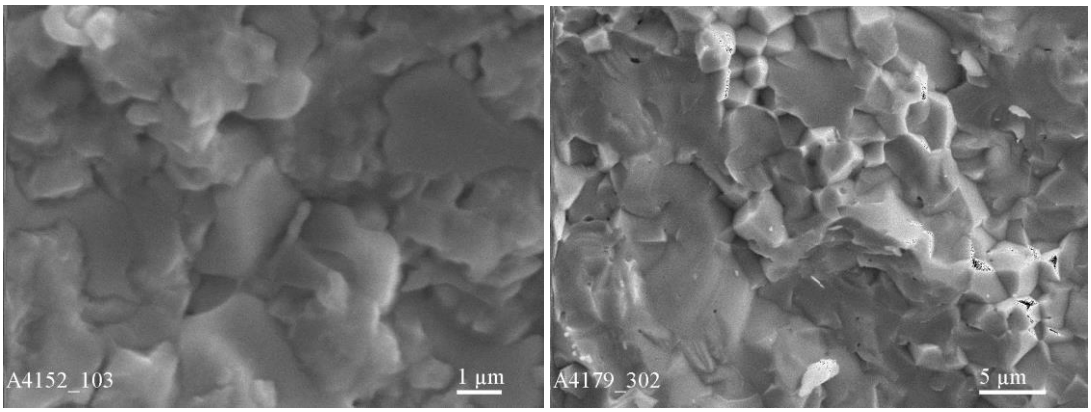

Figure 9. Microstructure of the sintered $LaLuO_3$:Yb^{3+} (2 mol%) sample by SPS at 1380 °C and annealed at 1100 °C for 4 h of the: a) not polished surface and b) fracture surface

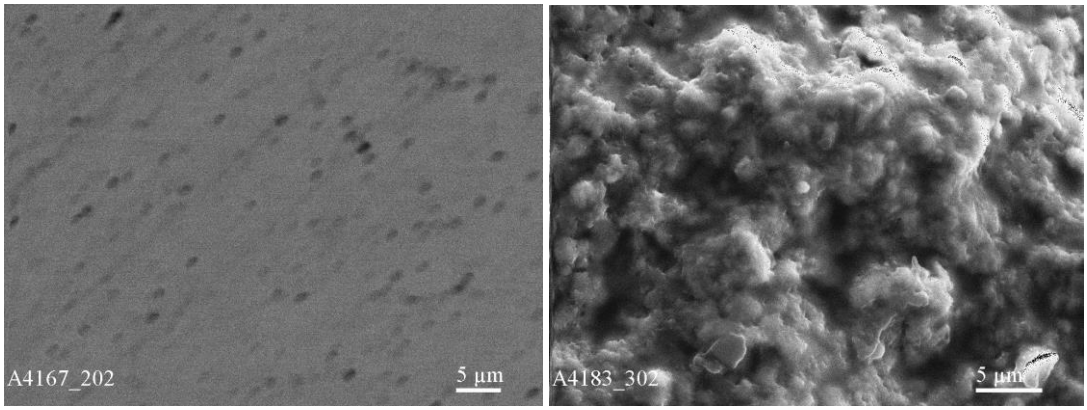

Figure 10. Microstructure of the sintered $LaLuO_3$:Yb^{3+} (2 mol%) sample by SPS at 1380 °C and annealed at 1100 °C for 24 h of the: a) polished surface and b) fracture surface

Microstructural studies also revealed that the single-phase sintered sample has very small portion of pores on the polished surface (Fig. 8a). Due to the low porosity, fracture of the sample occurs through the grain, which make it difficult to determine of the grain size after sintering (Fig. 8b).

The dark colour of the spark plasma sintered sample in graphite die in vacuum was supposed related to oxygen defects in the oxide lattice. Thus, annealing in air was carried out at temperature of 1100 °C for 4 or 24 h, which enabled restoration of white colour of the sample. After annealing, the sample underwent a slight reduction of weight and increase in density of ρ = 8.162 g/cm^3, corresponding to 99.54 %TD (of the theoretical maximum). Subsequent X-ray phase analysis (T = 1100 °C, 24 h) of the sample revealed no alterations in its phase composition (Fig. 7). The unit cell parameters of the annealed sample are as follows: a = 0.6013 nm, b = 0.8380 nm, c = 0.5822 nm and V = 0.2934 nm^3, and the average crystallite size and XRD density are D_{xrd} = 107.9 nm and ρ_{xrd} = 8.194 g/cm^3, respectively. It is evident that during the sintering and subsequent annealing processes, the size of the coherent scattering field increases from 51.2 to 108 nm.

The results of microstructural studies of the annealed ceramics indicate that, in contrast to the sintered sample, fracture of the sample occurs not only through the grain boundaries but also through the grains. Upon annealing at temperature of 1100 °C for 4 h, the formation of grains with a size ranged from 1.8 to 3.9 µm is observed (Fig. 9b). Hence, considering the SEM results of the nanopowder used for sintering, it can be inferred that the employed sintering regime leads to an increase in grain size from approximately 41 nm (Fig. 3) to approximately 1.8–3.9 µm (Fig. 9b). It is interesting to mention that with prolonging the annealing time to 24 h, the fracture surface structure changes and the fracture occurs along the grain (Fig. 10b).

Increasing the annealing temperature to 1250 °C results in the formation of a heterophase sample, which is undesirable. According to the results of the XRD phase analysis, the sample contains 3.2% of the cubic structure of C-Lu_2O_3. The microstructure of the investigated sample after thermal etching allows for the clear identification of the grain structure. The results obtained demonstrate that annealing leads to the formation of a dense structure with a minimal number of pores, primarily located at the grain interface and intragranular pores within large grains

(Fig. 11a). The investigated sample is characterized by the formation of grains ranging from 1.5 to 6.2 μm and pores measuring between 0.3 and 0.95 μm. It is noteworthy that pores of a smaller size, not exceeding 0.3 μm, are observed to form on the fracture surface of the sample.

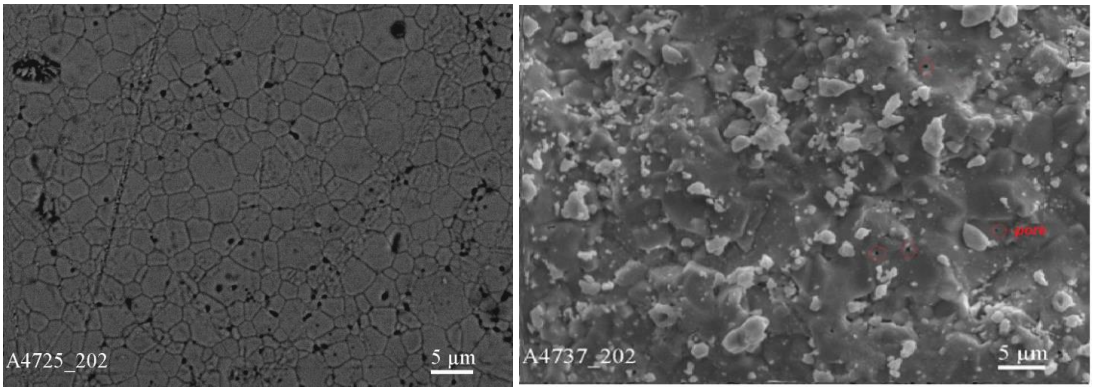

Figure 11. Microstructure of the sintered $LaLuO_3:Yb^{3+}$ (2 mol%) sample by SPS at 1380 °C, 15 min. Followed by annealing in air at 1250 °C (2 h): a - surface, b - fracture surface of the sample.

Varghese *et al*. [40] sintered an ordered phase, such as $LaLuO_3$ perovskite, in a muffle furnace under air atmosphere at temperatures of 1475 and 1525 °C for 4 h and obtained ceramic samples exhibited a relative density of 87.5 and 96 %TD, respectively. Thus, in the presented study, using the SPS method for sintering nanopowders with a perovskite-type structure, we managed to develop a sintering regime that produced a ceramic material with relative density of ~99.54 %TD. In addition, Varghese *et al*. [40] reported that sintering at 1525 °C causes the formation of large grains, i.e. from 5 to 10 μm. At the same time, in our case sintering by SPS method at 1380 °C produces structure with much smaller grains, ~1.8–3.9 μm.

Further research in improving sintering regime, which will enable formation of optically transparent fine-grained $LaLuO_3:Yb^{3+}$ ceramics, will be focused on both reduction of input particle size and better control of the pore size distribution on the final stage sintering to reduce sintering temperature.

V. Conclusions

This work resulted in the development of a methodology for synthesising nanopowder based on an ordered phase with a $LaLuO_3$ perovskite-type structure doped with Yb^{3+} ions. Infrared spectroscopy revealed the peaks at ν ~ 468 and 501 cm^{-1}, indicating the crystallisation of the ordered perovskite-type structure, and XRD analyses confirmed the formation of single-phase $LaLuO_3:Yb^{3+}$ (2 mol%) structure. The obtained nanopowder exhibits narrow particle size distribution ranging from approximately 41 to 60 nm. The resulting nanopowder was densified by spark plasma sintering. It was found that the spark-plasma sintering method can produce a dense material (density >99 %TD) at heat treatment temperatures of 1380 °C and pressing pressure of 50 MPa. Subsequent annealing in air was carried out at temperature of 1100 °C for 4 or 24 h, which enabled restoration of white colour of the sample. After annealing, the sample underwent a slight reduction of weight and increase in density of ρ = 8.162 g/cm^3, corresponding to 99.54 %TD.

Acknowledgement: The work was carried out under NATO project No. 56 G 5769 “Laser Ceramics for Detector of Harmful Substances” and contract No. M/57-2023 dated 25.08.2023

References

1. A. Ashok, A. Kumar, R.R. Bhosale, F. Almomani, S.S. Malik, S. Suslov, F. Tarlochan, “Combustion synthesis of bifunctional $LaMO_3$ (M = Cr, Mn, Fe, Co, Ni) perovskites for oxygen reduction and oxygen evolution reaction in alkaline media”, *J. Electroanal. Chem*., **809** (2018) 22–30.
2. N.A. Noor, U. Anwar, A. Mahmood, “Investigation of the rare earth-based $LaYO_3$ (Y = Cr and Mn) perovskites by ab-initio approach”, *Chem. Phys. Lett*., **739** (2020) 137031.
3. S.J. Schneider, R.S. Roth, “Phase equilibria in systems involving the rare-earth oxides. Part II. Solid state reactions in trivalent rare-earth oxide systems”, *J. Res. Nat. Bur. Stand A Phys. Chem*., **64A** (1960), 317–332.
4. H. Meller-Buschbaum, P. Graebne, “Zur Krirtallstruktur von $LaErO_3$ und $LaLuO_3$”, *Zeitschrift Anorg. Allgem. Chemie*, **386** (1971) 158–162.
5. G.Z. Zhang, X.-Z. Song, X.-F. Wang, N. Liu, X. Li, Z. Wei, G. Qian, Z. Wang, S. Yu, Z. Tan, “$LnFeO_3$ (Ln, La, Nd, Sm) derived from bimetallic organic frameworks for gas sensor”, *J. Alloys and Comp*., **902** (2022), 163803.
6. F.H. Gecit, S. Cabuk, “Structure and electronic properties of $LnScO_3$ compounds: A GGA+U calculation”, *Comput. Mater. Sci*., **208** (2022) 111350.
7. B.K. Downing, S.M. Hnatko, T. De Forest, E.L. Brosha, J. Valdez, R. Bloom, J. Smith, B.P. Uberuaga, B.L. Musico, “Synthesis of inter-lanthanide sesquioxides

LnLn'O_3 by polymeric steric entrapment", *J. Am. Ceram. Soc.*, **108** [10] (2025) e70024.
8. S.W. Kuk, S.-J. Ha, Y.W. Choe, J.-Y. Park, K. Jeong, S. Oh, K. Kim, S.-G. Park, J.H. Joo, W.S. Shin, K. Chang, "Development of $LaYO_3$ as a reaction-preventing material for metal fuel casting", *Int. J. Refrac. Met. Hard Mater*., **119** (2023) 106536.
9. K.L. Ovanesyan, A.G. Petrosyan, G.O. Shirinyan, C. Pedrini, L. Zhang, "Czochralski single crystal growth of Ce- and Pr-doped $LaLuO_3$ double oxide", *J. Cryst. Growth*, **198/199** (1999) 497–500.
10. A.V. Kasyanova, J.G. Lyagaeva, G.K. Vdovin, A.A. Murashkina, D.A. Medvedev, "Transport properties of $LaYbO_3$-based electrolytes doped with alkaline earth elements", *Electrochim. Acta*, **439 (**2023) 141702.
11. W. Zhang, Y.H. Hu, "Progress in proton-conducting oxides as electrolytes for low-temperature solid oxide fuel cells: from materials to devices", *Energy Sci. Eng.*, **9** (2021) 984–1011.
12. M. Boubchir, H. Aourag, "Materials genome project: Mining the ionic conductivity in oxide perovskites", *Mater. Sci. Eng: B*, **267 (**2021) 114984.
13. M. Tryus, K.V. Nikolaev, I.A. Makhotkin, Jü. Schubert, L. Kibkalo, S. Danylyuk, A. Giglia, P. Nicolosi, L. Juschkin, "Optical and structural characterization of orthorhombic $LaLuO_3$ using extreme ultraviolet reflectometry", *Thin Solid Films*, **680 (**2019) 94–101.
14. Yu. Yurchenko, O. Shyrokov, O. Korniienko, V. Laguta, Z. Remes, S. Zazubovich, A. Ragulya, T. Lobunets, "X-ray diffraction, luminescence, and electron paramagnetic resonance study of $LaLuO_3$:Yb^{3+} nanopowders", *Ceram. Int*., **50** (2024) 55008–55016.
15. S. Kalusniak, C. Guguschev, R. Koc, D. G. Schlom, C. Kränkel, "Efficient long wavelength laser operation and spectroscopic characterization of Yb:$LaLuO_3$", *Laser Congress 2024 (ASSL, LAC, LS&C)*, Technical Digest Series (Optica Publishing Group, 2024), paper ATh3A.6.
16. H. Liu, J. Cheng, H. Dong, J. Feng, B. Pang, Z. Tian, Sh. Ma, F. Xia, Ch. Zhang, L. Dong, "Screening stable and metastable ABO_3 perovskites using machine learning and the materials project", *Compu. Mater. Sci*., **170** (2020) 109614.
17. U. Kazushige, T. Syuto, Y. Takuma, Sh. Yuhei, H. Tetsuo, "Site-selective doping and site-sensitive photoluminescence of Eu^{3+} and Tb^{3+} in perovskite-type $LaLuO_3$", *Inorg. Chem*., **58** (2019) 10890–10897.
18. Sh. Nagashima, K. Ueda, T. Omata, "Site-dependent Tb^{3+} luminescence by energy transfer from Ce^{3+} in Ce^{3+}-Tb^{3+} codoped $LaLuO_3$", *J. Phys. Chem. C*, **126** (2022) 6499−6504.
19. O. V. Chudinovych, O.I. Bykov, A.V. Samelyuk, "Phase relation studies in the La_2O_3-Lu_2O_3-Yb_2O_3 system at 1500 °C", *J. Chem. and Technol*., **29** (2021) 485–494.
20. O.A. Kornienko, O.V. Chudinovych, A.I. Bykov, A.V. Samelyuk, E. R. Andrievskaya, "Phase equilibria in the La_2O_3–Er_2O_3 system in the temperature range 1100–1500°C", *Powder Metall. Met. Ceram*., 58 (2019) 89–98.
21. M.K. Mahata, K. Kumar, V.K. Rai, "Structural and optical properties of Er^{3+}/Yb^{3+} doped barium titanate phosphor prepared by co-precipitation method", *Spectrochim. Acta Part A: Molec. Biomolec. Spectrosc*. **124** (2014), 285–291.
22. Y. Sakabe, Y. Yamashita, H. Yamamoto, "Dielectric properties of nano-crystalline $BaTiO_3$ synthesized by micro-emulsion method", *J. Eur. Ceram. Soc*., **25** (2005) 2739–2742.
23. X. Zhu, J. Zhu, S. Zhou, Z. Liu, N. Ming, D. Hesse, "$BaTiO_3$ nanocrystals: Hydrothermal synthesis and structural characterization", *J. Cryst. Growth*, **283** (2005) 553–562.
24. T. Kimura, Q. Dong, S. Yin, T. Hashimoto, A. Sasaki, T. Sato, "Synthesis and piezoelectric properties of Li-doped $BaTiO_3$ by a solvothermal approach", *J. Eur. Ceram. Soc*., **33** (2013) 1009–1015.
25. S.H. Jhung, J.-H. Lee, J.W. Yoon, Y.K. Hwang, J.-S. Hwang, S.-E.Park, "Effects of reaction conditions in microwave synthesis of nanocrystalline barium titanate", *Mater. Lett*., **58** (2004) 3161–3165.
26. K.K. Lee, Y.C. Kang, K.Y. Jung, J.H. Kim, "Preparation of nano-sized $BaTiO_3$ particle by citric acid-assisted spray pyrolysis", *J. Alloys Compd*., **395** (2005) 280–285.
27. B. Kwak, K. Zhang, E. Boyd, A. Erbil, B. Wilkens, "Metalorganic chemical vapor deposition of $BaTiO_3$ thin films", *J. Appl. Phys*., **69** (1991) 767–772.
28. A.M. Huízar-Félix, T. Hernández, S. de la Parra, J. Ibarra, B. Kharisov, "Sol-gel based Pechini method synthesis and characterization of $Sm_{1-x}Ca_xFeO_3$ perovskite $0.1 \leq x \leq 0.5$", *Powder Technol*., **229** (2012) 290–293.
29. M. Niznanský, K. Vanmeensel, J. Vleugels, V. Tyrpekl, M. Vilemova, "Review on high-pressure spark plasma sintering and simulation of the impact of die/punch material combinations on the sample temperature homogeneity", *Open Ceram*., **16** (2023) 100433.
30. D. Salvato, "Innovative preparation route for uranium carbide using citric acid as a carbon source", *Ceram. Int*., **42** (2016) 16710–16717.
31. V.G. Kolesnichenko, M.V. Zamula, Y.V. Yurchenko, "Spark plasma sintering of magnesium fluoride nanopowders", *Powder Metal. Metal. Ceram*., **58** (2019) 406–415.
32. P. Šolcová, "Preparation of high-entropy (Ti, Zr, Hf, Ta, Nb) carbide powder via solution chemistry", *Inorg. Chem*., **60** (2021) 7617–7621.
33. A. Ragulya, "Consolidation of ceramic nanopowders", *Adv. Appl. Ceram*., **107** (2008). 118–134.
34. K. Ito, K. Tezuka, Y. Hinatsu, "Preparation, magnetic susceptibility, and specific heat on interlanthanide perovskites ABO_3 (A=La-Nd, B=Dy-Lu)", *J, Solid State Chem*,, **156** (2001) 173–179.
35. J. I. Langford, A.J.C. Wilson, "Scherrer after sixty years: A survey and some new results in the determination of crystallite size", *J. Appl. Crystallogr*., **11** (1978) 102–113.
36. A. Karnaukhov, *Adsorption. Texture of Dispersed and Porous Materials*, Nauka, Novosibirsk, 1999.
37. S. Brunauer, *Adsorption of Gases and Vapors*, 1948.
38. S. Greg, K. Singh, *Adsorption, Specific Surface Area, Porosity*, 1948.
39. I.M. Fedorchenko, R.A. Andrievsky, *Fundamentals of Powder Metallurgy*, Kiev: AN, 1961, p. 353.
40. J. Varghese, T. Joseph, M.T. Sebastian, N. Reeves-McLaren, A. Feteira, "Crystal structure and microwave dielectric properties of $LaLuO_3$ ceramics", *J. Am. Ceram. Soc*., **93** (2010) 2960–2963.